nature astronomy

Article

https://doi.org/10.1038/s41550-023-02038-1

Landing site of the Chang'e-6 lunar farside sample return mission from the Apollo basin

Received: 14 September 2022

Accepted: 26 June 2023

Published online: 31 July 2023

Check for updates

Xingguo Zeng[1,6], Dawei Liu[1,6], Yuan Chen[1,6], Qin Zhou[1], Xin Ren[1], Zhoubin Zhang[1], Wei Yan[1], Wangli Chen[1], Qiong Wang[2], Xiangjin Deng[3], Hao Hu[2], Jianjun Liu[1,4], Wei Zuo[1,4] ✉, James W. Head[5] ✉ & Chunlai Li[1,4] ✉

To address questions about the multiple lunar nearside–farside dichotomies and to provide new insights into both the early impact history of the Solar System and the geological evolution of the Moon, the Chang'e-6 (CE-6) landing zone has been selected to lie within the lunar farside South Pole–Aitken (SPA) basin in the southern part of the Apollo basin (150–158° W, 41–45° S), a site that provides access to a diversity of SPA material. Here, we describe the geomorphology, geology and chronology of three candidate sampling sites within this zone that are likely to ensure safe landing and sampling. The geological characteristics indicate that CE-6 is expected to collect lunar farside SPA ejecta fragments, possible mantle material and young (roughly 2.40 Gyr-year-old) and/or old (roughly 3.43 Gyr-year-old) basaltic material, all of which will provide important guidance for future in situ farside sample collection and deepen our understanding of the evolution of the Moon.

The South Pole–Aitken (SPA) basin, located on the lunar farside, consistently ranks as the highest priority site for sample return on the Moon due to its unique combination of farside location, extremely large size, very ancient (but unknown) age, interior compositional anomalies and location of a wide age range of post-SPA farside mare volcanism. The striking lunar nearside–farside asymmetries have been recorded in differences in crustal thickness, geological age of surface units and features, thermal structure, global geochemistry, abundance of surface radioactive elements, nature of terranes, size and abundance of impact basins, fundamental crustal structure and composition, and chronology. Despite these pronounced and enigmatic nearside–farside asymmetries, the fundamental questions they raise remain unresolved due to the lack of in situ samples returned from the lunar farside. These question include[1–8]: what is the lunar farside crustal composition and structure? What is the composition of the lunar mantle? What are the formation ages of the major farside and/or limb impact basins? What is the origin of the nearside Procellarum-KREEP Terrain and what are the implications for early lunar history? What is the mineralogy, geochemistry, chronology and mode of eruption of mare basalts on the lunar farside? The huge expanse of the SPA basin (roughly 2,400 km diameter) means that many human and/or robotic sample return missions will be required to address all of the key sampling priorities related to these questions (for example, 1–3). Nonetheless, recent robotic sampling of lunar soils (Chang'e-5) has clearly demonstrated that less than 2 kg of returned lunar soil can effectively sample and characterize a wide region and address many outstanding scientific problems. As a first step in an international SPA basin sample return campaign, China's CE-6 mission has chosen to land in the southern part of the 490 km diameter Apollo peak-ring basin that formed inside the SPA basin, excavated SPA basin ejecta, farside highlands and possibly mantle material, and which contains several postbasin farside mare deposits of different ages. Thus, the Apollo basin ejecta and interior deposits provide access to landing sites that are highly likely to contain a range of fragments that will help to characterize the main chronological and

[1]Key Laboratory of Lunar and Deep Space Exploration, National Astronomical Observatories, Chinese Academy of Sciences, Beijing, China. [2]Lunar Exploration and Space Engineering Center, Beijing, China. [3]Beijing Institute of Spacecraft System Engineering, Beijing, China. [4]School of Astronomy and Space Science, University of Chinese Academy of Sciences, Beijing, China. [5]Department of Earth, Environmental and Planetary Sciences, Brown University, Providence, RI, USA. [6]These authors contributed equally: Xingguo Zeng, Dawei Liu, Yuan Chen. ✉e-mail: zuowei@nao.cas.cn; James_Head@brown.edu; licl@nao.cas.cn

https://doi.org/10.1038/s41550-023-02038-1

composition characteristics of SPA and the lunar farside, and help to sharpen specific questions and destinations for future missions (see the Supplementary Information for a brief description and the landing site selection of the CE-6 mission).

Geological characteristics of the CE-6 landing zone

The current landing zone is determined by both engineering constraints and scientific questions to lie in the southern half of the Apollo basin rim in the northeast interior of the SPA basin (Fig. 1). SPA is the largest (roughly 2,400 km), deepest (roughly 6.2–8.2 km) and oldest (roughly 4.3 Gyr old) impact basin known on the Moon[9–12]. Numerical modelling studies suggest that the SPA basin may have excavated to depths reaching the lunar mantle[3,13], and SPA mantle-derived ejecta is likely to have been diluted, obscured and redistributed by later geologic processing[6,14]. Nonetheless, the material composition of the surface of the SPA basin is unique, showing iron and thorium anomalies as well as pyroxene-dominated mineralogy[4,6,15]. SPA has been divided into four approximately concentric mineralogical annuli[4]. From inner to outer annulus, the composition of pyroxene shows a trend from slightly Ca- and Fe-rich pyroxene to Mg-pyroxene, and a decreasing trend in pyroxene abundance and increase in plagioclase abundance.

The 490 km Apollo basin, formed roughly 3.9–4.1 billion years ago (Ga), is located in the northeast interior, just inside the SPA basin[16]. This specific location may make the northeastern Apollo rim more feldspathic and the southwestern rim more noritic[15]. Previous studies[17–22] have shown that the interior of the Apollo basin contains both residual material from impact events and volcanic products (basalts, cryptomare and floor-fracture craters and so on). Apollo was probably outside the SPA transient cavity, and may have excavated entirely through the Th-bearing SPA ejecta deposit, so that the ejected deep materials from the SPA-forming impact could have been locally removed by the formation of Apollo basin 6 but may still reside on the basin rim and walls. In addition, some noritic pyroxene compositions within the Apollo basin (for example, Dryden crater) may be more Mg-rich than other noritic materials across SPA[23,24], which could be associated with a deep lower crust or even mantle materials excavated by the Apollo-forming impact[23].

The CE-6 landing zone (Fig. 1a,b), is located at the boundary between the central region SPA compositional anomaly (SPACA) (a resurfacing unit dominated by Ca- and Fe-rich pyroxene that may be cryptomare and/or non-mare volcanic materials[19,25]) and Mg-pyroxene-rich annulus[4], providing a high possibility of collecting a diverse set of samples. This area has an average slope of roughly 5.74°, and the total area with slopes below 8° (the maximum slope for safe landing) accounts for 76% of the total area, making this region favourable for landing. A total of 26,785 craters (diameters of more than 50 m) were identified within the CE-6 landing zone (Fig. 2a). Greater than 96% are between 100 m and 1 km in diameter. Secondary craters, rays and crater chains, important for enhancing returned sample diversity and final site selection strategy, are scattered in the CE-6 landing zone and marked by their locally higher albedo and characteristic morphology (Fig. 3a). Crater chains show a generally northeast–southwest distribution, but the directions of some apparent secondary crater clusters are uncertain. Two types of positive landform are observed in the mare

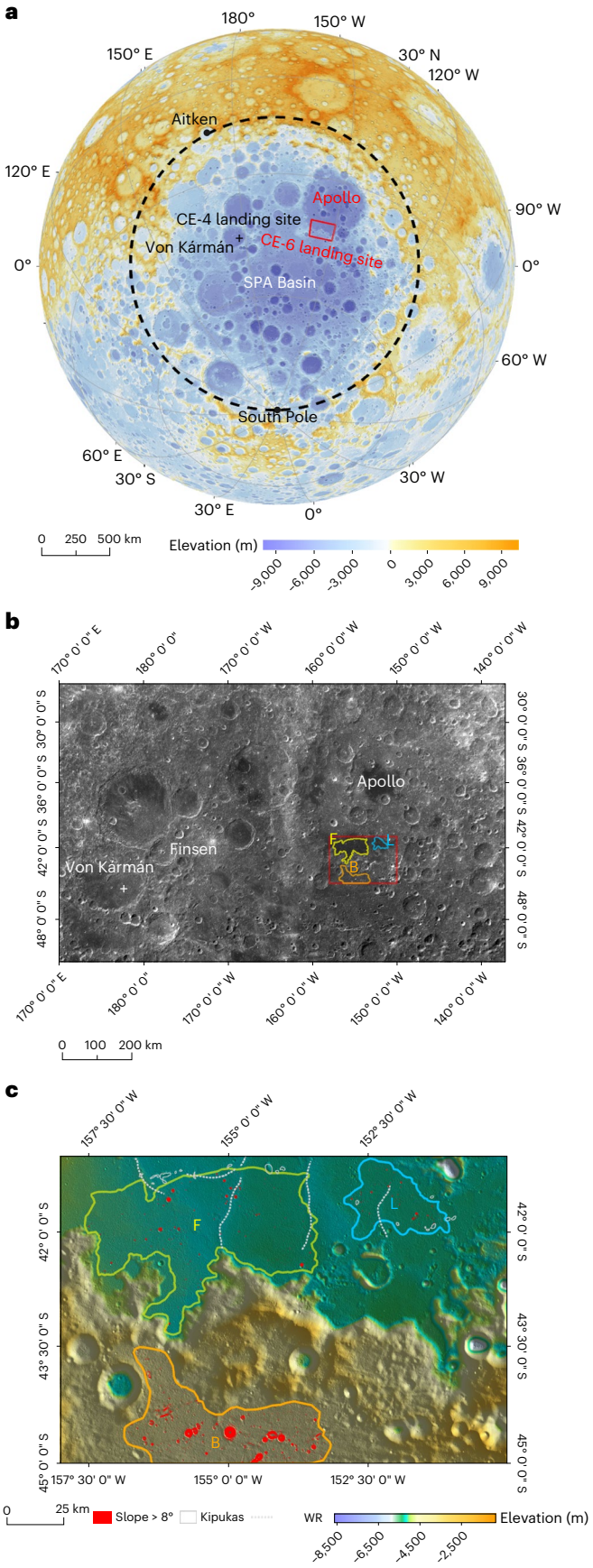

Fig. 1 | The CE-6 landing region. a, Location and topographic features on the lunar farside: the SPA basin is outlined by a black dashed line; the CE-6 landing zone is outlined by a red box and the cross indicates the CE-4 landing site. Base map is a shaded-relief map from CE-1 DEM data. **b**, The CE-6 landing zone, located in the SPA basin interior along the southern rim of the Apollo basin (CE-2 DOM image). The albedo shows the distribution of basaltic (low albedo) and non-basaltic (higher albedo) materials in the zone. **c**, Topographic and morphological map of the proposed CE-6 sampling regions; region F (yellow solid line) represents the northwest plain, region L (blue solid line) the northeast lowland and region B (orange solid line) represents the southwest Apollo basin rim. The kipukas and WR are distributed in the F and L areas. Base map comes from CE-2 DEM data (20 m per pixel).

https://doi.org/10.1038/s41550-023-02038-1

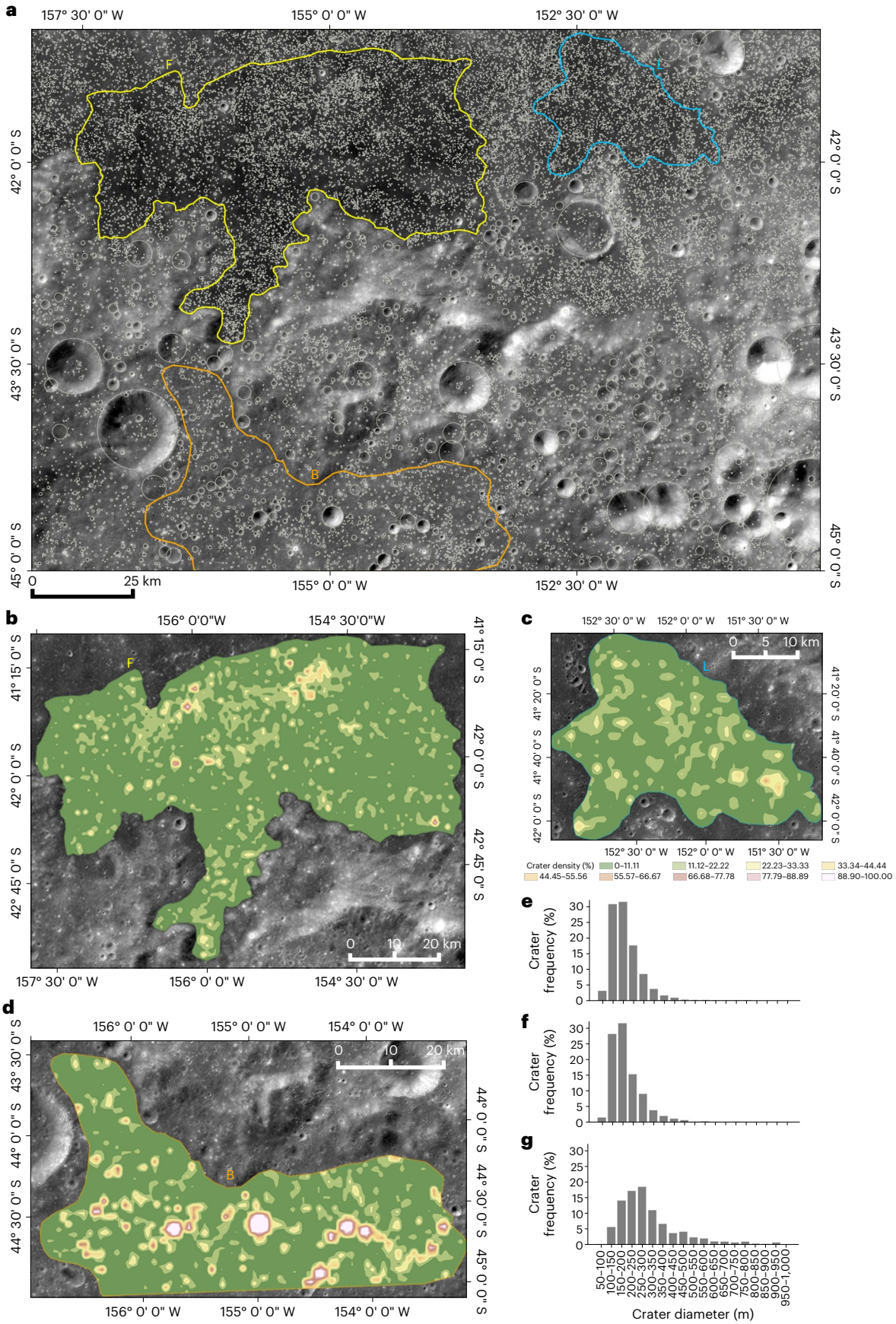

Fig. 2 | The distribution of impact craters (diameter more than 50 m) in the candidate CE-6 sampling sites. a, The distribution of craters in the entire landing zone. **b**–**d**, Crater densities in the three candidate sampling sites, F (**b**), L (**c**) and B (**d**). The crater density is the percentage of area occupied by impact craters within a surface area of 1 km^2. **e**–**g**, Diameter-frequency distribution of craters in the candidate sampling regions of F (**e**), L (**f**) and B (**g**).

plains (Fig. 1c): (1) kipukas, remnants of the Apollo basin floor and wall structures (or rims of pre-mare superposed craters) that protrude through the mare lavas, and (2) wrinkle ridges (WRs), interpreted as tectonic shortening features formed subsequent to emplacement of the lava flows[26,27].

Within this zone, we have identified three relatively flat regions favoured by engineering operational constraints (Fig. 1b,c): region F (northwest flat plain, designated F), region L (northeast low plain, designated L) and region B (southwest base plain, designated B). Following final region selection, a safe site for landing will be selected during descent and postlanding in situ analysis and sample collection will occur.

Topography, geomorphology and chronology

Region F (Figs. 1c, 2b and 3b,e) is a mare patch located between the rim crest and the peak ring of the Apollo basin. The overall topography slopes slightly to the east (Fig. 1c). Craters occupy roughly 8.61% of the area (fewer than ten craters more than 1 km diameter) (Fig. 2b,e). The relatively flat terrain (average elevation −5,197 m, slope 2.36°) and the lower abundance of craters suggest that this region is suitable for safe landing and sampling. The importance of superposed crater ejecta deposits can be quantified by the average ejecta index (Methods), a measure of normalized relative grey value to the dark mare basalt. Region F has an average ejecta index of 0.34 (Fig. 3e), and the ejecta is spread unevenly on the surface of the low-albedo basalts. Several linear ejecta patterns are oriented northwest–southeast (Fig. 3a,b) and northeast–southwest (Figs. 1b and 3b). WRs (Fig. 1c) can be recognized in region F; they do not extend to the wall or floor of the Apollo basin, indicating their association with postmare basalt emplacement deformation. They are arrayed both radially and circumferentially to the centre of the Apollo basin (Fig. 1c), in a manner similar to WR distribution in the Orientale basin[28]. Region F is mapped as the late-Imbrian unit in the United States Geological Survey geologic map[29], and Upper Imbrian dark plain in Ivanov's geomorphological map[20] (Fig. 4a). This basaltic region has been previously dated as roughly 2.44 (ref. 30), 3.63 (ref. 31) and 3.31 Gyr old (ref. 21), respectively. Our crater size frequency distribution (CSFD) results within F_A (Fig. 4e) reveal that absolute model ages (AMA) for the basaltic unit of F is roughly 2.40 Gyr (Eratosthenian), among the youngest maria on the farside (Fig. 4e and Extended Data Fig. 1).

Region L is a mare patch located east of region F (Figs. 1c, 2c and 3c,f) and separated from region F by a higher-albedo zone. The area occupied by craters is 10.36% (three craters more than 1 km diameter) (Fig. 2c,f). The average elevation, −5,277 m, and slope of roughly 2.37° are similar to those of region F, which makes region L suitable for safe landing and/or sampling. The region L ejecta index is 0.66 (Fig. 3f). Bright ejecta is more densely spread over the basaltic background in the L region than in region F, and the distribution is relatively uniform with a faint northwest–southeast distribution trend (Fig. 3c). Some partly buried craters exist at the boundary between regions F and L dark mare patches and the Apollo basin wall, suggesting that the dark mare basalts may have filled the post-Apollo basin, pre-mare impact craters. WRs (Fig. 1c) can also be observed; the largest WR (Extended Data Fig. 2) at the boundary of the F and L region modified the L basalt surface and impeded the F basaltic flow. This suggests that F and L basalts erupted during two separate periods, with F basalts formed later than the L basalts (Methods and Extended Data Figs. 2 and 3). Region L is also mapped as the late-Imbrian unit[29] and Upper Imbrian dark plain[20] (Fig. 4a). Previous studies have dated this basaltic region as roughly 2.44 (ref. 30), 3.63 (ref. 31) and 3.45 Gyr old (ref. 21). CSFD results reveal that AMA for the basalts where region L is located is roughly 3.43 Gyr (Imbrian) (Fig. 4e and Extended Data Fig. 1), much older than the region F basalts. This indicates that basalts within the F and L mare regions occur in at least two different time periods (roughly 2.40 and 3.43 Ga) (consistent with WR observations), and thus samples will provide important information on farside volcanic age, composition and mantle diversity.

Region B is a higher-albedo plain unit located on the southern Apollo basin rim (Figs. 1c, 2d and 3d,g), with an average elevation of about −4,172 m, roughly 1,000 m higher than that of regions F and L. The overall topography of region B is flat, but slightly higher in the east and west and lower in the central area. Region B has a slightly higher average slope (3.59°) than region F (roughly 2.36°) and L (2.37°). The areal percentage occupied by craters is 12.71% (46 craters more than 1 km diameter) (Fig. 2d,g). Compared to the region F and L mare patches, region B is a more typical unit in the interior of the SPA basin such as SPACA[4]. Candidate sources and modes of origin include Apollo basin ejecta, SPA basin interior impact melt and cryptomare as well as non-mare volcanic materials. Region B has been mapped as an Imbrian-Nectarian basin unit[29] and an Imbrian light plain unit[20] (Fig. 4a). We obtained an AMA for region B and the surrounding flat area (B_A) (Fig. 4e and Extended Data Fig. 1) of roughly 3.86 Gyr, very slightly younger than the roughly 3.98 Gyr AMA obtained for the Apollo impact basin by Ivanov et al.[20]. Interpretation of this AMA depends on the genesis of the materials in region B. If this unit is an Apollo basin impact ejecta deposit, this age will reflect the age of the Apollo basin and the crystallization age of its rock materials is very likely to be older and at least partly composed of SPA basin material.

Predicted characteristics of CE-6 returned samples

Large-scale geological mapping, stratigraphic reconstructions and spectroscopic analyses suggest that F and L are composed of mare basalt substrates and laterally mixed ejecta materials from adjacent non-mare sources. By contrast, region B appears to be a unit bearing Fe- and Ca-rich pyroxene, resurfaced by cryptomare, Apollo basin ejecta and/or SPACA non-mare volcanic material[4–6,25]. We performed detailed spectral analysis (Methods) of the three candidate sampling regions (Fig. 5) using Moon Mineralogy Mapper (M^3) data to better understand compositions and potential sample provenance.

Region F is a relatively pristine mare basalt area, with a lower abundance and more limited distribution of non-mare ejecta materials from adjacent areas (Fig. 3b). Spectral analysis of fresh craters (Fig. 5b) in this relatively pristine basalt area show that the mare basalts of region F have obvious absorption features of pyroxene and appear to be dominated by Fe- and Ca-rich clinopyroxene (absorptions centre in transition area from pigeonite to augite, Fig. 5b). Compared to the spectra of mare basalts of the nearside Oceanus Procellarum CE-5 landing site, band centres of region F mare basalts are slightly shifted towards short wavelengths, indicating lower Fe and Ca content of pyroxenes in region F basalts compared to CE-5 basalts. Spectral features and Ti and Fe contents of region F suggest the dominance of typical mare basalts and local regolith provenance. Lunar samples returned from region F could be very pristine mare basalts with a proportion of laterally mixed foreign ejecta even less than that of CE-5 samples. The CSFD dating result for F region is roughly 2.40 Gyr (Fig. 4e and Extended Data Fig. 1), interpreted to represent the crystallization age of region F mare basalts. The AMA of region F mare basalt is older than CE-5 samples (roughly 2.0 Gyr old) and younger than the Apollo mission basalt samples, and thus samples from region F will provide an extremely valuable calibration point for CSFD chronology and understanding of farside mantle and the thermal evolution of the Moon.

The region L Mare basalt unit has been affected strongly by lateral mixing of non-mare material from adjacent source craters (Fig. 3c). Region L fresh craters spectra show absorption features dominated by clinopyroxene, but with their 1 and 2 μm band centre (Fig. 5b) shifted towards short wavelengths compared to that of the F region craters (Fig. 5b). This may indicate that the average pyroxene Fe and Ca contents of region L mare basalts are lower than that of region F mare basalts. It is worth noting that the overall chemical composition of region F basalts is notably higher in Fe and Ti than that of region L basalts (Figs. 4b,c). This may imply a weakening of a typical 'basalt

https://doi.org/10.1038/s41550-023-02038-1

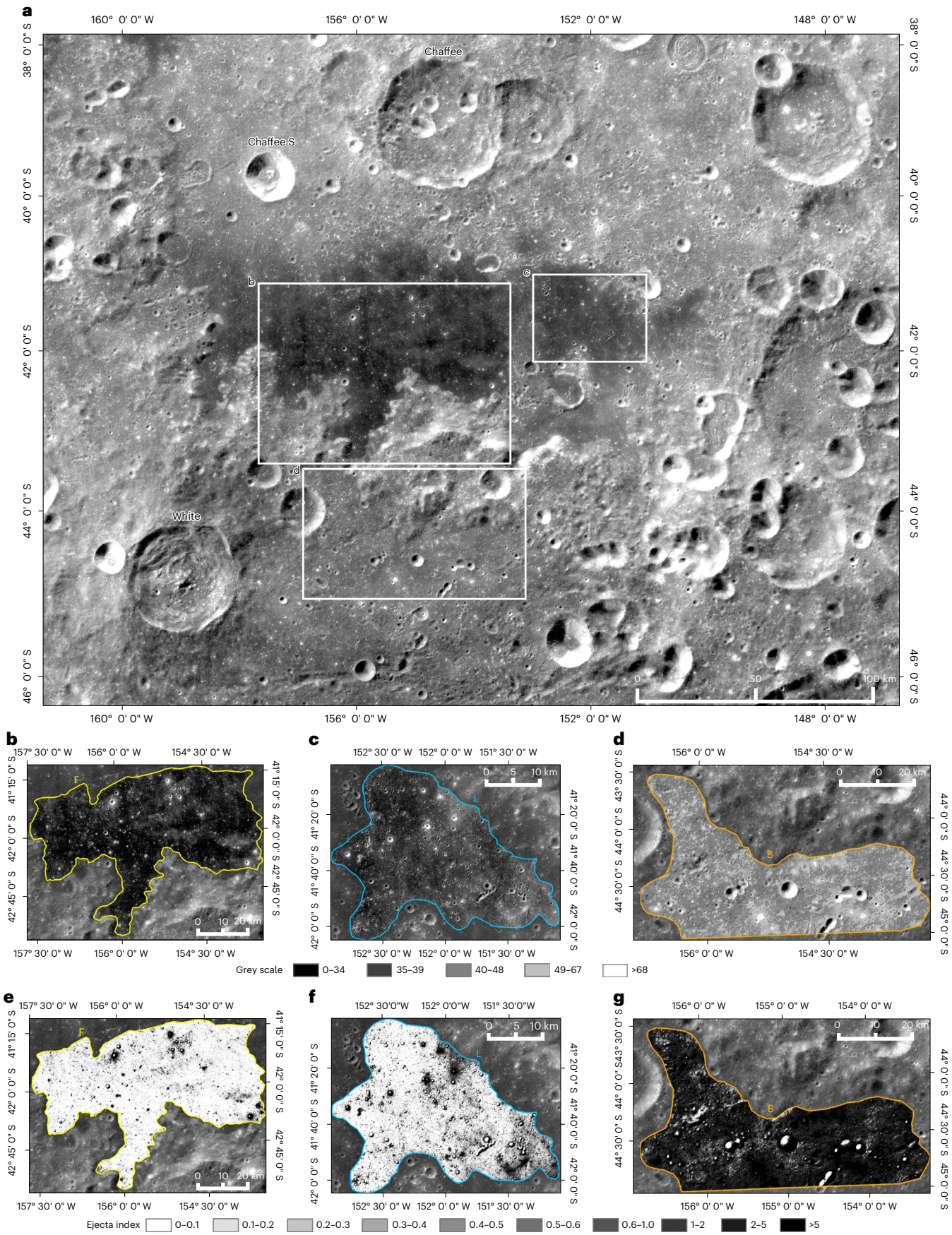

Fig. 3 | The distribution of lateral ejecta (for example, rays, crater chains and clusters) in the candidate sampling sites. a, The distribution of ejecta within the entire landing zone. **b**–**d**, The distribution of ejecta in the F (**b**), L (**c**) and B (**d**) candidate sampling regions. **e**–**g**, The ejecta index of F (**e**), L (**f**) and B (**g**) candidate sampling regions (Methods). All the base maps are from CE-2 DOM image data.

https://doi.org/10.1038/s41550-023-02038-1

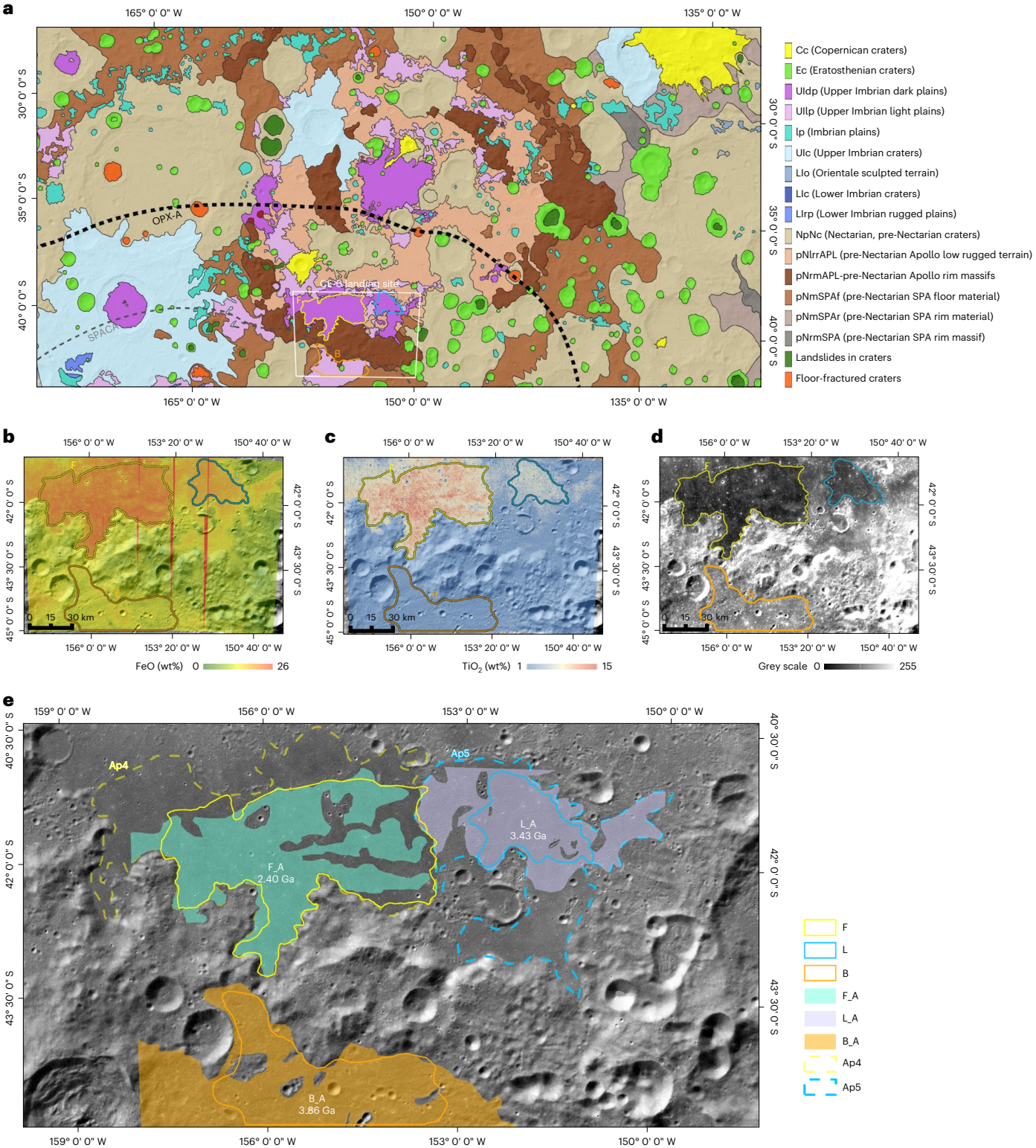

Fig. 4 | Geological context, units and structure of the northeast SPA basin and the CE-6 candidate landing zone and sampling regions in the Apollo basin and on its southern rim. a, Regional geological map of the northeast SPA and the Apollo basin, modified from Ivanov et al.[20]. **b**, FeO content distribution of the candidate sampling region derived from Multiband Imager (MI) data[48]. **c**, TiO_2 content distribution of the candidate sampling region derived from LRO WAC data[49]. **d**, The relative albedo distribution of the candidate sampling regions based on CE-2 DOM data. **e**, Geological units and CSFD dating results for the candidate sampling regions in this study, Ap4 (yellow dashed line) and Ap5 (blue dashed line) are CSFD areas defined by ref. 21. Solid lines represent the three candidate regions (F, L and B). The coloured regions (F_A, L_A and B_A) are the areal extent for CSFD dating in this study.

geochemical signature' due to the lateral mixing of non-mare ejecta materials. It is likely that materials of region L are more obviously mixed with the non-mare mafic components ejected from the Apollo basin floor (Fig. 5a) and/or its eastern rim (Fig. 5a). In terms of material composition, the Apollo basin floor and its eastern rim display short-wavelength absorptions dominated by Mg-rich pyroxene (for

https://doi.org/10.1038/s41550-023-02038-1

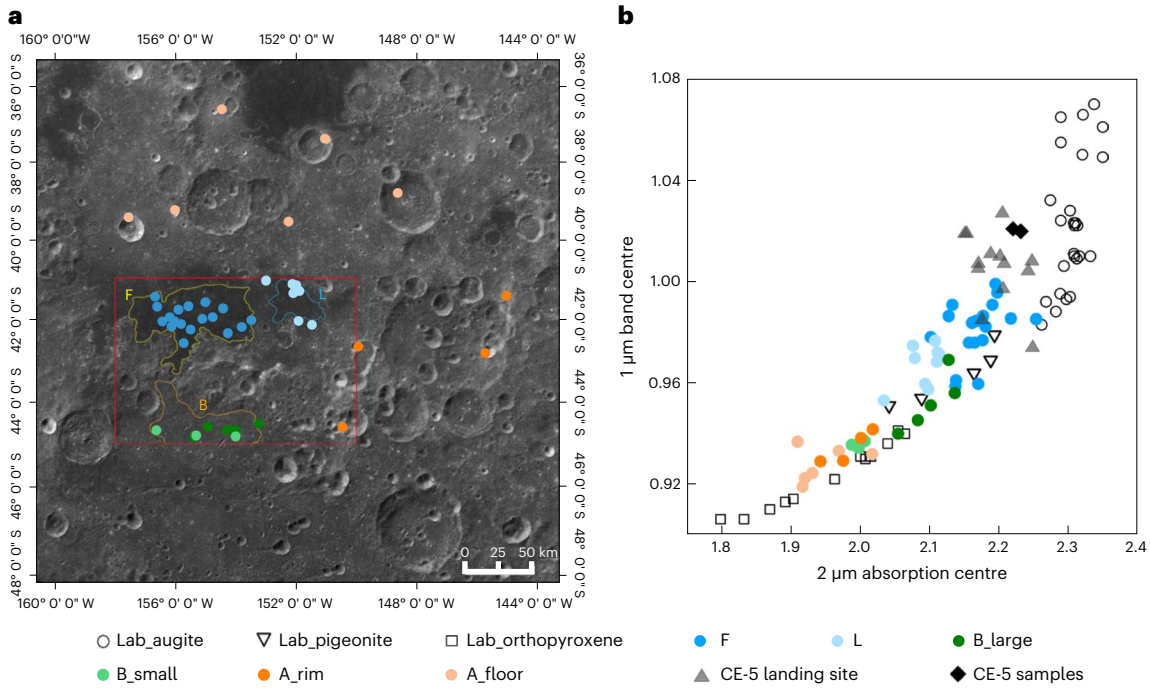

Fig. 5 | Spectral analysis of CE-6 landing area. a, The locations of fresh craters used in the spectral analysis. Base map from CE-2 DOM. **b**, The absorption centres of pyroxene of varying composition (1 versus 2 μm); blue solid circle, samples of F; light blue solid circle, samples of L; dark green solid circle, samples of B (large craters); light green solid circle, samples of B (small craters); light orange solid circle, Apollo inner ring floor; orange solid circle, Apollo east outer rim; solid triangle, mare basalts of the CE-5 landing area; solid diamond, CE-5 returned samples; black hollow circle, laboratory (lab) measured augite; hollow triangle, laboratory measured pigeonite and hollow square, laboratory measured orthopyroxene. Data for F, L, B, Apollo inner ring floor, Apollo outer rim and CE-5 mare basalts were derived from M^3 orbital data. Data for CE-5 samples and lab measured pyroxene are from Liu and Wang et al.[47] and Klima et al.[50], respectively. The spectrum analysis method is similar to ref. 47 (Methods).

example, orthopyroxene) (Fig. 5b). The overall material composition tends to be more noritic[15,32]. Subsequent impact events will eject materials from these regions (for example, Apollo basin floor and rim) onto the surface of L mare basalts, laterally mixing with them, resulting in increased albedo and reflectance and a shift in the spectral absorption centres towards short wavelengths. Samples returned from region L should contain a mixture of primarily mare basalt materials, admixed with noritic materials laterally emplaced from adjacent non-mare source craters. The interpreted crystallization age of region L basalts should be around 3.43 Gyr (Fig. 4e and Extended Data Fig. 1).

Large craters in region B (Fig. 5b) exhibit an intermediate (pigeonite-like) average pyroxene composition, similar to that of region L mare basalts (Fig. 5b). At the same time, the spectra of some small craters (Fig. 5b) within region B show absorption features typical of orthopyroxene, and similar to those observed on the non-mare portions of the Apollo basin floor (Fig. 5a) and the eastern Apollo basin rim (Fig. 5a). These noritic-composition materials dominated by orthopyroxene could represent ejecta materials delivered to region B by surrounding impact craters or, alternatively, the surface unit and/or materials characteristic of region B. Combining the longer wavelength absorption features and an apparent decrease in the number of craters in the SPACA region, Moriarty and Pieters[4,6,19,25,33] inferred that the Ca, Fe-rich materials in region B are likely to be gabbroic volcanic resurfacing deposits, bearing mineralogy similar to the mafic mound in SPACA but distinct from typical mare basalts, which suggests a unique and local thermal and magmatic history. These resurfacing deposits were then covered by more noritic Apollo ejecta[25]. Region B's roughly 3.86 Gyr AMA surface unit age may also represent the age of the Apollo basin (estimated at roughly 3.98 Gyr by Ivanov et al.[20]), as suggested by its surface compositional similarities to Apollo basin floor and wall units. In this case, rocks and soil material from region B could contain material ejected from Apollo basin and/or surrounding impact basins and/or craters. In addition, a new type of unknown volcanic resurfacing deposit, possibly represented by Ca, Fe-rich gabbroic materials excavated by large craters, could be sampled within this region.

Discussion and conclusions

In summary, CE-6 could collect (1) from region F lunar farside mare basalt and a small amount of non-mare ejecta, (2) from region L farside mare basalts and a higher abundance of non-mare ejecta and (3) from region B Apollo basin ejecta materials and probably a new type of previously unsampled volcanic resurfacing deposit.

Mare basalts in region F have an age close to 2.40 Gyr old (younger Eratosthenian), and mare basalts in region L are dated at roughly 3.43 Gyr old (Imbrian). On the basis of CSFD dating studies, lunar nearside mare activity spanned a time interval from roughly 3.9–4.0 to 1.2 Ga (ref. 34,35). Most of the volcanisms on the lunar farside occurred between 3.0 and 3.6 Ga, with a few deposits dating to roughly 2.5 Ga (refs. 30,36–38). The cessation of volcanism on the lunar farside appears to be much earlier than that on the lunar nearside[39,40]. So far, no direct evidence has been found for farside volcanic activity between 2.2 and 2.5 Ga or younger[21]. If samples returned by CE-6 can confirm the age of basalt samples in these regions to be less than 2.5 Gyr, this will extend the farside mare basalt generation to time more similar to the nearside, a potential finding of great importance for understanding the thermal evolution of the Moon. The age of available Apollo samples is in the range of 3.1–3.9 Gyr old, and the youngest age provided by CE-5 basalt samples is 2.0 Gyr old (ref. 41). CE-6 mare basalt chronology will play a key role in the continued refinement of the CSFD curve. In addition, mare basalt samples acquired by CE-6 (regions F and L) will contribute to addressing the questions of the nature of farside mantle source regions, lunar volcanism nearside–farside asymmetry and the role of crustal thickness in ascent and eruption[39,40].

Analysis of all farside samples (regions F, L and B) permits the assessment and testing of the distribution of radioactive elements, the origin of the Procellarum-KREEP Terrane and the role of the SPA basin impact in inducing convective transport of a KREEP layer from the farside to the nearside and causing nearside–farside asymmetries in Th and Ti (for example, refs. 8,42,43).

It is highly probable that CE-6 will acquire ejecta materials (dominant in region B and secondary ejecta in mare regions F and L), including ejecta originating from the Apollo rim and wall that may contain some contributions of SPA ejecta and also craters within the Apollo basin interior. Apollo has probably penetrated through and removed the SPA ejecta deposit, which is distinctive due to its high Th abundance and a potential uppermost mantle origin[6]. However, such materials are still likely to be preserved in the Apollo basin wall and rim, especially the southern rim with noritic composition and relatively high Th abundance; these could easily be excavated and redistributed within the landing zone by subsequent impact craters. In addition, outcrops originating from deep-seated layers (lower crust or even mantle) may also appear in the Apollo interior[18], especially the most Mg-rich noritic materials found near the western peak ring[23,24]. Subsequent impact craters targeting this region may also bring ejecta to the CE-6 landing zone. The crystallization age of returned ejecta materials is likely to exceed 3.9 Gyr, and will provide fundamental information on the timing of the SPA and Apollo impact events, greatly improving knowledge of the impact chronology of the Moon and the entire inner solar system. Acquisition of any deep crustal and possible mantle materials by CE-6 will also revolutionize our thinking about the composition of the lunar interior, the thermal evolution of the Moon and the role of original lunar accretional source materials following the Moon-forming Earth impact event.

Methods

Calculation of the ejecta index

The ejecta index (EI), defined to describe the degree of pollution by impact ejecta, with an assumption that ejecta material could make the dark basalt area brighter in digital orthophoto model (DOM) image data[44], is a mathematical method using transformation of the DOM image grey value (0–255) into an index (0–100) based on a base value (Grey_Base, GB). GB is a grey value of the purest basalt in the same geological unit (for example, the same phase of basaltic cover) in the study area (and is therefore considered to be the lowest).

Then, for each pixel of a DOM image:

$$\text{If grey value} <= \text{GB}, \text{EI} = 0$$

$$\text{If grey value} > \text{GB}, \text{EI} = (\text{grey value} - \text{GB})/(255 - \text{GB}) \times 100$$

Pixels with grey value higher than the GB, are considered to be ejecta material with different pollution levels. Then, for the average EI(EI_AVG) of a region:

$$\text{EI\_AVG} = \text{Sum(EI\_All)}/\text{Pixel\_Num}$$

where Sum (EI_ALL) represents the summary of EI of all pixels in the region, and Pixel_Num represents the number of pixels.

Chronology of candidate landing regions

To better constrain the age of regions F, L and B, we first excluded areas that include large clusters and chains of secondary craters on the basis of the distribution of Fe (Fig. 4b), Ti (Fig. 4c) contents and ejecta (Fig. 4d). Then, we used the software ArcMap CraterTools[45] to map and count the craters of the geological units where the candidate landing regions are located on the basis of CE-2 DOM images, and the obvious secondary craters were excluded from the counted areas. Finally, the CSFD dating curves were derived with software CraterStats[46], and the results are shown in Extended Data Fig. 1.

Morphological and compositional observations about the formation sequence of F and L regions

Extended Data Fig. 2 is a CE-2 digital elevation model (DEM) topographic map, and the elevated terrain in the middle is a WR. Extended Data Fig. 2b is a Lunar Reconnaissance Orbiter Camera Wide Angle Camera (LROC WAC) normalized three-band false-colour image, in which the dark basalt locates in the F region and the less dark basalt is within the L region with clear boundaries. Referring to the low-sun illumination LROC WAC image (Extended Data Fig. 2c), the WR here is divided into two sections in the south (S) and north (N) for separated discussion. From Extended Data Fig. 2b,c, we can see that the south section WR (S-WR) does not perfectly coincide with the southeast boundary of the F basalts. S-WR locates within the dark basalt and is roughly 20 m above the mare surface; we assume that S-WR could only have been deformed and uplifted after the basalt overflow, otherwise, the dark basalts would not be able to cover the S-WR surface. We extracted the contours of the area using CE-2 DEM data and found that the east boundary of the F dark basalt is highly coincident with the baseline (−5,260 m contour) of the northern WR (N-WR) (Extended Data Fig. 2c,d), which we interpret to mean that the N-WR blocked the eastwards flow of the basalt in the F region, and further means that the N-WR existed before the basalt overflow in the F region.

The composition map data (Extended Data Fig. 3) show that the materials on the N-WR surface are similar to that of the L region. Their hues are fairly consistent on the WAC normalized three-band map, Clementine false-colour composite image, M^3 data, Fe and Ti element distribution map, respectively, so we believe that the N-WR surface is mainly composed of basalts similar to that of the L region. It is assumed that N-WR was not yet completely elevated when the L basalts flowed, and less dark basalts of the L region accumulated nearby. Then, the N-WR uplifted and formed a high topographic barrier. Later, when the F basalts erupted, the N-WR blocked the dark basalt from flowing eastwards, so the eastern boundary of the F basalts fits almost completely with the basal contour of the N-WR.

Spectrum analysis of candidate landing regions

The M^3 spectral data shorter than 2,497 nm were used in this study. They were first smoothed using the Savitzky–Golay method to reduce the noise. Then, a two-straight-lines method was adopted for the continuum removal of all M^3 spectra. The two straight lines were set at tangents to the left and right sides of the absorption bands. For roughly 1 μm absorption, the left tangent point varied from 600 to 800 nm, and the right tangent point varied from 1,300 to 1,800 nm. One point was taken in each of these two ranges iteratively. When the straight line joining the two points completely covered the 1 μm absorption band, it was treated as the tangent line of the roughly 1 μm absorption band. The tangent line of the 2 μm band was found using the same method. The left tangent point varied between 1,300 and 1,800 nm and the right endpoint was set at 2,497 nm. The continuum-removed M^3 spectrum was obtained by dividing the reflectance of each band by the corresponding value of the tangent line. After this, a fourth-order polynomial was used to fit the continuum-removed M^3 spectrum around 1 and 2 μm absorptions. The wavelengths corresponding to the minimums of the fitted lines are regarded as the band centres of the spectrum. This band centre derivation method was the same as that used by Liu and Wang et al.[47].

Data availability

The CE-1 and CE-2 data used in this work were processed and produced by the GRAS of China's Lunar and Planetary Exploration Program, provided by China National Space Administration (https://moon.bao.ac.cn). The geologic map data of CE-6 landing site were accessed from https://data.planmap.eu/pub/moon/PM-MOO-MS-SPAApollo/. The MI FeO content data were accessed from https://astrogeology.usgs.gov/search/map/Moon/Kaguya/MI/MineralMaps/

Lunar_Kaguya_MIMap_MineralDeconv_FeOWeightPercent_50N50S. The LRO TiO_2 content data were accessed from https://wms.lroc.asu.edu/lroc/view_rdr/WAC_TIO2. The M^3 data were accessed from https://pds-imaging.jpl.nasa.gov/volumes/m3.html. The data used in this paper are available at https://moon.bao.ac.cn/Moon/CE6-landingsite.rar and/or https://doi.org/10.12350/CLPDS.GRAS.CE6.AD-LandingSite.v202304. Datasets generated or analysed during this study are available from the corresponding author upon reasonable request. Source data are provided with this paper.

References

1. National Research Council (NRC). *Scientific Context for the Exploration of the Moon* (National Academies Press, 2007).
2. Jolliff, B. L., Gillis, J. J., Haskin, L. A., Korotev, R. L. & Wieczorek, M. A. Major lunar crustal terrains: surface expression and crust-mantle origins. *J. Geophys. Res.* **105**, 4197–4216 (2000).
3. Melosh, H. et al. South Pole–Aitken basin ejecta reveal the Moon's upper mantle. *Geology* **45**, 1063–1066 (2017).
4. Moriarty, D. P. & Pieters, C. M. The character of South Pole-Aitken basin: patterns of surface and subsurface composition. *J. Geophys. Res. Planets* **123**, 729–747 (2018).
5. Moriarty, D. P., Dygert, N., Valencia, S. N., Watkins, R. N. & Petro, N. E. The search for lunar mantle rocks exposed on the surface of the Moon. *Nat. Commun.* **12**, 4659 (2021).
6. Moriarty, D. P. et al. Evidence for a stratified upper mantle preserved within the South Pole-Aitken Basin. *J. Geophys. Res. Planets* **126**, e2020JE006589 (2021).
7. Pieters, C. M. & Head, J. W. Sampling the South Pole-Aitken Basin: outstanding issues and opportunities for international lunar exploration. In 53th *Proc. Lunar and Planetary Science Conference* 1682 (Lunar and Planetary Institute, 2022).
8. Jones, M. J. et al. A South Pole–Aitken impact origin of the lunar compositional asymmetry. *Sci. Adv.* https://doi.org/10.1126/sciadv.abm8475 (2022).
9. Fassett, C. et al. Lunar impact basins: stratigraphy, sequence and ages from superposed impact crater populations measured from Lunar Orbiter Laser Altimeter (LOLA) data. *J. Geophys. Res. Planets* **117**, E00H06 (2012).
10. Garrick-Bethell, I. & Zuber, M. T. Elliptical structure of the lunar South Pole-Aitken basin. *Icarus* **204**, 399–408 (2009).
11. Spudis, P. D., Gillis, J. J. & Reisse, R. A. Ancient multiring basins on the Moon revealed by Clementine laser altimetry. *Science* **266**, 1848–1851 (1994).
12. Stuart-Alexander, D. E. *Geologic Map of the Central Far Side of the Moon* (US Geological Survey Report, 1978).
13. Potter, R. W. et al. Constraining the size of the South Pole-Aitken basin impact. *Icarus* **220**, 730–743 (2012).
14. Li, C. et al. Chang'E-4 initial spectroscopic identification of lunar farside mantle-derived materials. *Nature* **569**, 378–382 (2019).
15. Pieters, C. M. et al. Rock types of South Pole-Aitken basin and extent of basaltic volcanism. *J. Geophys. Res. Planets* **106**, 28001–28022 (2001).
16. Baker, D. M. et al. The transition from complex crater to peak-ring basin on the Moon: new observations from the Lunar Orbiter Laser Altimeter (LOLA) instrument. *Icarus* **214**, 377–393 (2011).
17. Baker, D. M. et al. The formation of peak-ring basins: working hypotheses and path forward in using observations to constrain models of impact-basin formation. *Icarus* **273**, 146–163 (2016).
18. Potter, R. W. K. et al. The Apollo peak-ring impact basin: insights into the structure and evolution of the South Pole–Aitken basin. *Icarus* **306**, 139–149 (2018).
19. Whitten, J. L. & Head, J. W. Lunar cryptomaria: physical characteristics, distribution, and implications for ancient volcanism. *Icarus* **247**, 150–171 (2015).
20. Ivanov, M. et al. Geologic history of the northern portion of the South Pole-Aitken basin on the Moon. *J. Geophys. Res. Planets* **123**, 2585–2612 (2018).
21. Pasckert, J. H., Hiesinger, H. & van der Bogert, C. H. Lunar farside volcanism in and around the South Pole–Aitken basin. *Icarus* **299**, 538–562 (2018).
22. Poehler, C. et al. Geological mapping of the South Pole-Aitken Basin region. In *Proc. Europlanet Science Congress 2020* Vol. 15, 646 (Europlanet Society, 2021).
23. Klima, R. L. et al. New insights into lunar petrology: distribution and composition of prominent low-Ca pyroxene exposures as observed by the Moon Mineralogy Mapper (M3). *J. Geophys. Res. Planets* **116**, E00G06 (2011).
24. Moriarty, D. P. & Pieters, C. M. Evaluation of stratigraphy at the South Pole-Aitken Basin: from local to regional. In 45th *Proc. Lunar and Planetary Science Conference* 1777 (Lunar and Planetary Institute, 2014).
25. Moriarty, D. P. et al. A preliminary evaluation of resurfacing scenarios across the South Pole—Aitken Basin interior from a mineralogical assessment of craters. *LPI Contributions* **2678**, 2386 (2022).
26. Sharpton, V. L. & Head, J. W. Lunar mare ridges: analysis of ridge-crater intersections and implications for the tectonic origin of mare ridges. In 18th *Proc. Lunar and Planetary Science Conference* 307–317 (Lunar and Planetary Institute, 1988).
27. Watters, T. R. Wrinkle ridge assemblages on the terrestrial planets. *J. Geophys. Res. Solid Earth* **93**, 10236–10254 (1988).
28. Yue, Z. et al. Global survey of lunar wrinkle ridge formation times. *Earth Planet. Sci. Lett.* **477**, 14–20 (2017).
29. Fortezzo, C. M., Spudis, P. D. & Harrel, S. L. Release of the digital unified global geologic map of the Moon at 1:5,000,000-scale. In 51st *Proc. Lunar and Planetary Science Conference* 2760 (Lunar and Planetary Institute, 2020).
30. Haruyama, J. et al. Long-lived volcanism on the lunar farside revealed by SELENE terrain camera. *Science* **323**, 905–908 (2009).
31. Greeley, R. et al. Galileo imaging observations of Lunar maria and related deposits. *J. Geophys. Res.* **98**, 17183 (1993).
32. Pieters, C. M. et al. Mineralogy of the mafic anomaly in the South Pole-Aitken basin: implications for excavation of the lunar mantle. *Geophys. Res. Lett.* **24**, 1903–1906 (1997).
33. Moriarty, D. P. & Pieters, C. M. The nature and origin of mafic mound in the South Pole-Aitken Basin. *Geophys. Res. Lett.* **42**, 7907–7915 (2015).
34. Hiesinger, H., Jaumann, R., Neukum, G. & Head, J. W. Ages of mare basalts on the lunar nearside. *J. Geophys. Res.* **105**, 29239–29275 (2000).
35. Hiesinger, H., Head, J. W., Wolf, U., Jaumann, R. & Neukum, G. in *Recent Advances and Current Research Issues in Lunar Stratigraphy* (eds Ambrose, W. & Williams, D. A.) 1–51 (Geological Society of America, 2011).
36. Morota, T. et al. Mare volcanism in the lunar farside Moscoviense region: implication for lateral variation in magma production of the Moon. *Geophys. Res. Lett.* **36**, 1–5 (2009).
37. Morota, T. et al. Timing and characteristics of the latest mare eruption on the Moon. *Earth Planet. Sci. Lett.* **302**, 255–266 (2011).
38. Morota, T. et al. Timing and duration of mare volcanism in the central region of the northern farside of the Moon. *Earth Planets Space* **63**, 5–13 (2011).
39. Head, J. W. & Wilson, L. Generation, ascentand eruption of magma on the Moon: new insights into source depths, magmasupply, intrusions and effusive/explosive eruptions (Part 2: predicted emplacement processes and observations). *Icarus* **283**, 176–223 (2017).

40. Wilson, L. & Head, J. W. Generation, ascent and eruption of magma on the Moon: new insights into source depths, magma supply, intrusions and effusive/explosive eruptions (Part 2: predicted emplacement processes and observations). *Icarus* **283**, 146–175 (2017).
41. Li, Q. L. et al. Two-billion-year-old volcanism on the Moon from Chang'E-5 basalts. *Nature* **600**, 54–58 (2021).
42. Zhang, N. et al. Lunar compositional asymmetry explained by mantle overturn following the South Pole-Aitken impact. *Nat. Geosci.* **15**, 37–41 (2022).
43. Hagerty, J. J., Lawrence, D. J. & Hawke, B. R. Thorium abundances of basalt ponds in South Pole-Aitken basin: insights into the composition and evolution of the far side lunar mantle. *J. Geophys. Res. Planets* **116**, E06001 (2011).
44. Li, C. et al. Characteristics of the lunar samples returned by the Chang'E-5 mission. *Natl Sci. Rev.* **9**, 21–33 (2022).
45. Kneissl, T., van Gasselt, S. & Neukum, G. Map-projection-independent crater size-frequency determination in GIS environments—new software tool for ArcGIS. *Planet. Space Sci.* **59**, 1243–1254 (2011).
46. Michael, G. G. & Neukum, G. Planetary surface dating from crater size-frequency distribution measurements: partial resurfacing events and statistical age uncertainty. *Earth Planet. Sci. Lett.* **294**, 223–229 (2010).
47. Liu, D. et al. New spectral interpretation of late-stage mare basalt mineralogy unveiled by Chang'E-5 samples. *Submitted Nat. Commun.* **13**, 5965 (2022).
48. Lemelin, M. et al. Global map products from the Kaguya Multiband Imager at 512 ppd: minerals, FeO and OMAT. In 47th *Proc. Lunar and Planetary Science Conference* 2994 (Lunar and Planetary Institute, 2016).
49. Sato, H. et al. Lunar mare TiO_2 abundances estimated from UV/Vis reflectance. *Icarus* **296**, 216–238 (2017).
50. Klima, R. L., Dyar, M. D. & Pieters, C. M. Near-infrared spectra of clinopyroxenes: effects of calcium content and crystal structure. *Meteorit. Planet. Sci.* **46**, 379–395 (2011).

Acknowledgements

The Chang'e data used in this work were processed and produced by GRAS (Ground Research and Application System) of China's Lunar and Planetary Exploration Program. We also thank the Lunar Reconnaissance Orbiter (LRO), Kaguya, Chandrayaan and other related teams for providing the science data used in this paper. This study was funded by the Key Research Program of Chinese Academy of Sciences, grant no. ZDBS-SSW-JSC007 to C.L. and J.L., and funded by the National Natural Science Foundation of China, grant no. 12203073 to X.Z.

Author contributions

C.L., W.Z., J.L. and J.W.H. designed the research. X.Z., D.L., Y.C., Q.Z. and C.L. wrote the draft manuscript. X.Z., D.L. and Y.C. contributed equally to this work. C.L. and J.W.H. reviewed and finalized the manuscript. X.Z., W.Z. and Y.C. performed the topography, geology and chronology data analysis. D.L. and Y.C. conducted the spectrum data analysis. J.L., X.R., Z.Z., W.Y., Q.W., X.D., H.H. and W.C. conducted Chang'e data processing, calibration and validation.

Competing interests

The authors declare no competing interests.

Additional information

Extended data is available for this paper at https://doi.org/10.1038/s41550-023-02038-1.

Supplementary information The online version contains supplementary material available at https://doi.org/10.1038/s41550-023-02038-1.

Correspondence and requests for materials should be addressed to Wei Zuo, James W. Head or Chunlai Li.

Peer review information *Nature Astronomy* thanks Daniel Moriarty and the other, anonymous, reviewer(s) for their contribution to the peer review of this work.

https://doi.org/10.1038/s41550-023-02038-1

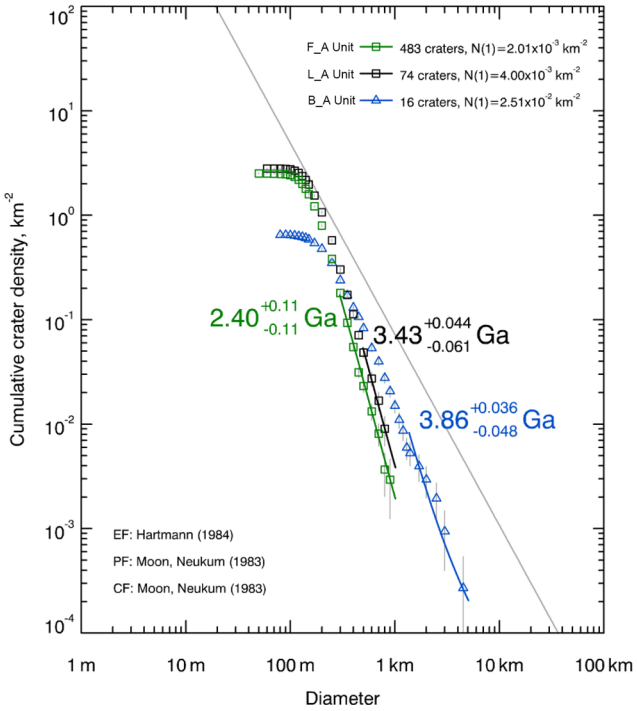

Extended Data Fig. 1 | Dating results of three sampling regions. CSFD dating curves for the geologic unit of the Candidate F, L and B sampling regions.

https://doi.org/10.1038/s41550-023-02038-1

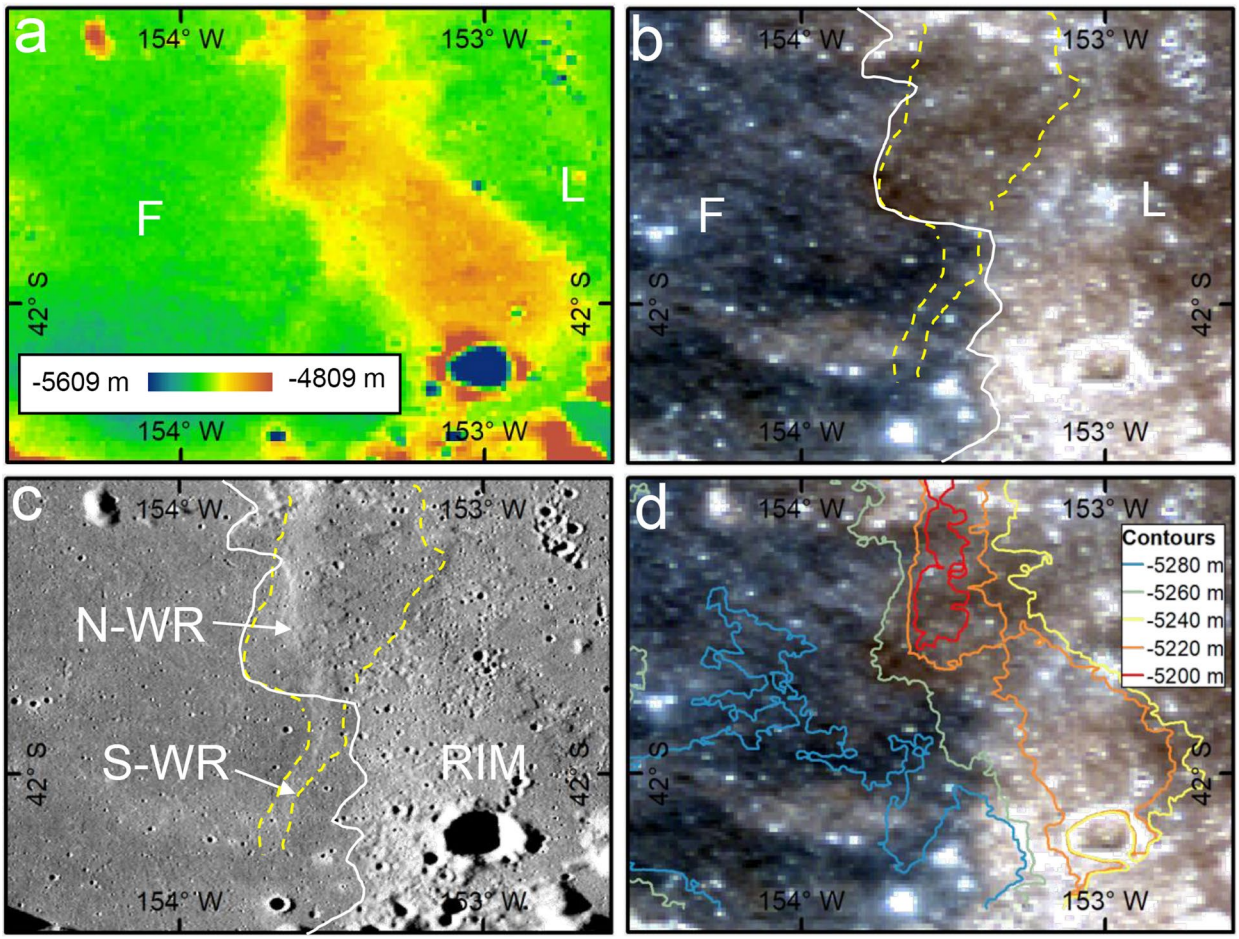

Extended Data Fig. 2 | Topographic boundaries of F and L regions. a) The CE-2 DEM topographic map. b) The LROC WAC normalized three band false-color image, yellow dashed lines are the wrinkle ridge. c)The low-sun illumination LROC WAC image. N-WR represents the northern wrinkle ridge, S-WR is the southern wrinkle ridge, and RIM is the area connected to the Apollo Basin rim. d) The 20 m interval contour which is contracted from CE-2 DEM data. The base map is LROC WAC false color image. It can be seen that the -5260 m contour, which represents the base of N-WR is highly consistent with the eastern boundary of the F basalts.

https://doi.org/10.1038/s41550-023-02038-1

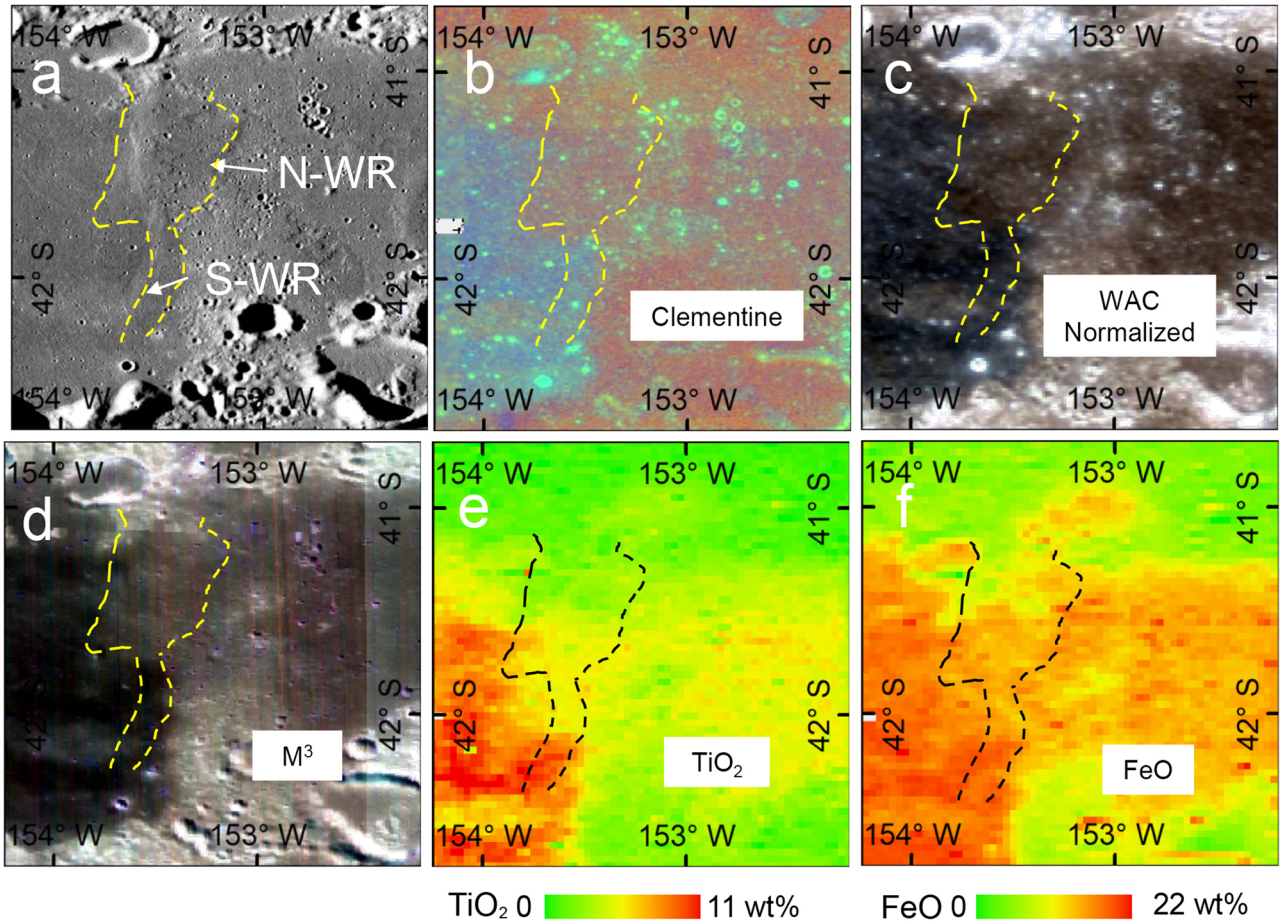

Extended Data Fig. 3 | Comparison of the surface material of the N-WR and the L basalts. The yellow dashed line marks the extent of the wrinkle ridge. The N-WR surface is generally consistent with the color hue of the L region in the Clementine false-color composite image, the LROC WAC normalized three-band color map, the M3 data, and the titanium and iron map, respectively.